# Local Temperature Determination of Optically Excited Nanoparticles and Nanodots

**3 AUTHORS**, INCLUDING:

Aurangzeb Khan

**40** PUBLICATIONS **291** CITATIONS

SEE PROFILE

Hugh Hill Richardson

Ohio University

**98** PUBLICATIONS **2,121** CITATIONS

SEE PROFILE

# Local Temperature Determination of Optically Excited Nanoparticles and Nanodots

Michael T. Carlson,[†] Aurangzeb Khan,[‡] and Hugh H. Richardson*,[†]

[†]Department of Chemistry and Biochemistry and [‡]Biomimetic Nanoscience and Nanoscale Technology Program (BNNT), Ohio University, Athens, Ohio 45701, United States

**S** *Supporting Information*

**ABSTRACT:** A thin film of $Al_{0.94}Ga_{0.06}N$ embedded with $Er^{3+}$ ions is used as an optical temperature sensor to image the temperature profile around optically excited gold nanostructures of 40 nm gold nanoparticles and lithographically prepared gold nanodots. The sensor is calibrated to give the local temperature of a hot nanostructure by comparing the measured temperature change of a spherical 40 nm gold NP to the theoretical temperature change calculated from the absorption cross section. The calibration allows us to measure the temperature where a lithographically prepared gold nanodot melts, in agreement with the bulk melting point of gold, and the size of the nanodot, in agreement with SEM and AFM results. Also, we measure an enhancement in the $Er^{3+}$ photoluminescence due to an interaction of the NP and $Er^{3+}$. We use this enhancement to determine the laser intensity that melts the NP and find that there is a positive discontinuous temperature of 833 K. We use this discontinuous temperature to obtain an interface conductance of ~10 MW/$m^2$-K for the gold NP on our thermal sensor surface.



**KEYWORDS:** Heat generation, gold nanoparticles, erbium photoluminescence, interface thermal conductance
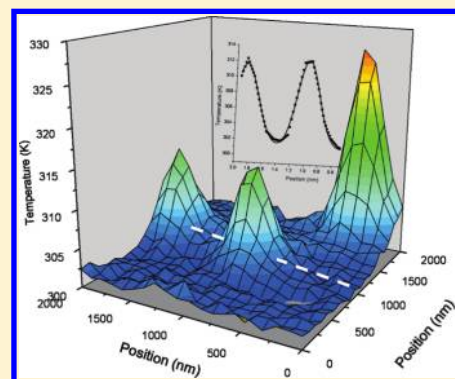
Nanoscale heat generation and dissipation impacts many fields of current research, including applications in medical therapies and the semiconductor industry, where device dimensions continue to be reduced as number densities increase. As device sizes approach the nanoscale, they become close in scale to the phonon mean-free path, where certain pathways for heat dissipation are less efficient. The classical heat diffusion law breaks down and the heat flow becomes ballistic.[1−3] Also in this regime, interfacial properties begin to dominate and limit the heat transfer away from the nanostructure.[4] Characterizing these interfacial properties and their impact upon heat dissipation is essential for an understanding of nanoscale heat transport.

An absorption measurement of nanostructures has the potential to be a more sensitive measurement over scattering because absorption scales as the volume instead of as volume squared.[5] This inherent sensitivity has motivated the development of a number of novel techniques that have been used to study isotropic and anisotropic nanostructures[5−12] in varied environments. Most of these techniques overcome the difficulty inherent to absorption measurements, where a small change in the transmitted light needs to be detected, by using modulated light. It is also possible to deduce the amount of light absorption by looking at an effect in the surrounding matrix.[13−18] Understanding the thermal transport from a flux of heat that crosses the nanostructure interface is key to relating the amount of light absorbed by the nanostructure to a temperature change in the surrounding medium.

In this paper we show that a novel optical thermal sensor can be used to measure the local temperature of a thin film with an optically excited gold nanostructure attached. The optical thermal sensor is made of a thin film of $Al_{0.94}Ga_{0.06}N$ incorporated with $Er^{3+}$. The sensor is used to determine the temperature of the film around either a single 40 nm gold nanoparticle (NP) or a single lithographically prepared nanodot during laser excitation. We are able to calibrate our sensor with the gold NP and predict the size, absorption cross section and melting temperature of the nanodot. Finally, we measure an enhancement in the $Er^{3+}$ photoluminescence due to an interaction of the NP and $Er^{3+}$. We use this enhancement to determine the laser intensity that melts the NP and find that there is a positive discontinuous temperature. We use this discontinuous temperature to obtain an interface conductance of ~10 MW/$m^2$-K for the gold NP on our thermal sensor surface.

**Experimental Section.** The thermal sensor consists of a thin film (~270 nm thick) of $Al_{0.94}Ga_{0.06}N$ embedded with $Er^{3+}$ ions on a silicon substrate. A layer of the $Al_{0.94}Ga_{0.06}N$ is deposited on the silicon substrate via RF magnetron sputtering.[19,20] The $Er^{3+}$ ions are excited with 532 nm laser light resulting in a typical $Er^{3+}$ photoluminescence spectrum (see Supporting Information, Figure S1). The relative intensities of the $^2H_{11/2} \rightarrow {}^4I_{15/2}$ and the $^4S_{3/2} \rightarrow {}^4I_{15/2}$ energy transitions of the $Er^{3+}$ ions have been shown to be temperature dependent.[19,21] These are related by a Boltzmann factor ($\exp(-\Delta E/kT)$ where $\Delta E$ is the energy

difference between the two levels, $k$ is the Boltzmann constant, and $T$ is the absolute temperature.

Two different nanostructures (solution synthesized NPs or lithographically made nanodots) are studied. Single, isolated, gold NPs are immobilized on the surface of the thermal sensor from suspended solutions. An ultrasonic processor (Sonics Vibra Cell 130 W 20 kHz) is used to clean the surface of dirt and organic particulates. The sample is placed in a small beaker of $CHCl_3$ and sonicated for 10 min at 50% amplitude. After sonication, the sample is removed from the $CHCl_3$ and dried with nitrogen gas. The sample is then transferred to a plasma cleaner/sterilizer (Harrick Scientific) under vacuum for 45 s to ensure complete removal of any lingering organic matter. Using an autopipette, poly-L-lysine is applied to the newly cleaned thin-film surface. The poly-L-lysine provides the first link in the chain to immobilize the gold nanoparticle on the surface. The plasma cleaning also changes the wettability of the surface to ensure sufficient adsorption of poly-L-lysine. Per manufacturer's packaged instructions, the sample is submerged in the poly-L-lysine for 5 min at room temperature. After 5 min, the sample is removed, and the excess is dried with nitrogen gas. Once completely dry, biotin (20 mM LC-Sulfo-NHS-Biotin (Pierce) solution) is bound to the surface by forming a peptide bond between the amine group of poly-L-lysine and the carboxyl group of the LC-Sulfo-NHS-Biotin molecule. The LC-Sulfo-NHS-Biotin solution is normally stored in the freezer and allowed to reach room temperature in a desiccator. After dilution, droplets of the biotin solution are placed on the thin film and allowed to sit for 45 min to ensure sufficient bonding. After 45 min, the excess is rinsed with ultrapure, 18 M$\Omega$ water and again dried with nitrogen gas. Once dried, a colloidal solution of Au nanoparticles (prepared by British Biocell International; purchased from Ted Pella) with an average diameter of 40 nm and coated with streptavidin is applied to the thin-film surface. The streptavidin-gold NP solution is diluted to a concentration (usually around $10^{10}$ particles/mL) to ensure that single particles are predominately immobilized on the surface. The diluted solution is then placed on the surface and allowed to sit for 45 min to again ensure sufficient attachment. After 45 min, the excess colloidal solution on the surface is rinsed with ultrapure, 18 M$\Omega$ water and dried with nitrogen gas. This procedure immobilizes predominately single Au NPs (confirmed by atomic force microscopy (AFM), see Supporting Information, Figure S2) by forming strong noncovalent bonds involving the streptavidin on the NP and biotin on the surface.

The gold nanodots are fabricated using conventional e-beam lithography with lift-off. We fabricated periodic arrays of Au dots of ∼120 nm in diameter and 50−70 nm in height using electron beam lithography. Single layers of around 100 nm of poly(methyl methacrylate) (PMMA) (3% PMMA 495 K in Anisole) positive resist were spin coated onto the $Al_{0.94}Ga_{0.06}N$/Er thin film on Si. The PMMA coated samples were baked in an oven for 30 min at 180 °C. After baking, electron beam lithography (∼30 KV in a JEOL 6400) was carried out to draw the desired pattern/dots arrays at the nanometer level. The samples were then developed with MIBK/IPA = 1:3 (volume) for 30 S and rinsed/cleaned with high purity water and then dried. A thin adhesion layer of Ti was first deposited then followed by a thicker (50−70 nm) layer of Au using DC sputtering. Lift-off procedure with laboratory grade acetone (heated at 60 °C) for 30 min with sonication was carried out in order to remove the Au/PMMA residual layer.

The optical temperature measurements using the thermal sensor with isolated gold nanostructures was made with a WITec α-SNOM300s upgraded with Raman imaging, dark-field, and
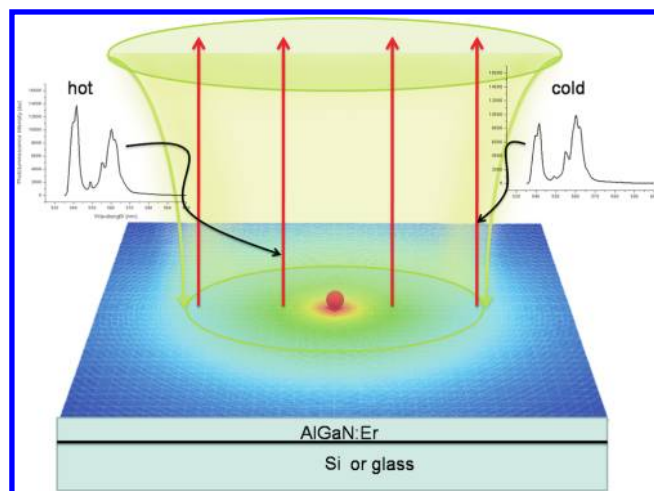


**Figure 1.** Diagram illustrating the properties of the thermal sensor. Excitation of a gold nanostructure with 532 nm light produces a hot spot whose temperature falls off as one over the distance. The photoluminescence spectrum from $Er^{3+}$ embedded in the thin film changes with temperature. Hotter temperatures increase the photoluminescence intensity of the higher energy peak at 540 nm relative to the lower energy peak at 565 nm (see Supporting Information, Figure S1).

AFM capabilities. A CW 532 nm wavelength YAG laser with adjustable power is focused with either a 50× dark-field objective (Zeiss EC-Epiplan-NEOFLUAR 50×/0.8 HD) or a 100× bright-field objective (Nikon Plan 100×/0.90 NCG) onto the thin film thermal sensor. The emitted light from the thermal sensor is collected with the same objective and sent to the CCD spectrograph with a collection fiber. The highest spatial resolution is achieved with a 25 $\mu$m collection fiber and most of the data in this paper has been collected with this fiber. The 50× objective used with the 25 $\mu$m collection fiber produced an Airy diffraction pattern that has a fwhm of ∼500 nm. This pattern was obtained by imaging in dark-field a small scattering object (single array dot). We used dark-field imaging and scattering to determine the location of the gold nanostructure on the thermal sensor (see Supporting Information, Figure S3). Once the location of the nanostructure is found and characterized, the thermal sensor is translated with nanometer control under the objective during laser excitation. An image is collected by storing the full photoluminescence spectrum at pixel locations within the image (100 pixels × 100 pixels). After storing a set of spectra, the image is constructed by processing the spectra for each pixel location. The temperature images are obtained by summing and baseline correcting a wavelength range corresponding to the $^2H_{11/2} \rightarrow$ $^4I_{15/2}$ and the $^4S_{3/2} \rightarrow {}^4I_{15/2}$ energy transitions. A ratio of the peak areas are then placed in the Boltzmann equation to produce a temperature that is dependent upon the value of the intercept. A calibration curve (Supporting Information, Figure S4) was generated to confirm that the relative peak intensities are related by a Boltzmann factor. The intercept is chosen so that the temperature in the limit of no laser intensity is room temperature.

The laser spot on the thermal sensor is calibrated for power and profile characteristics before data collection. The laser power ($P_{laser}$) is adjusted with a micrometer set screw that partially blocks the laser and is calibrated with an optical power meter (gentec TPM-300). The laser profile was determined using a camera to image the total photoluminescence emission from the thermal sensor at low laser power. The resulting image was
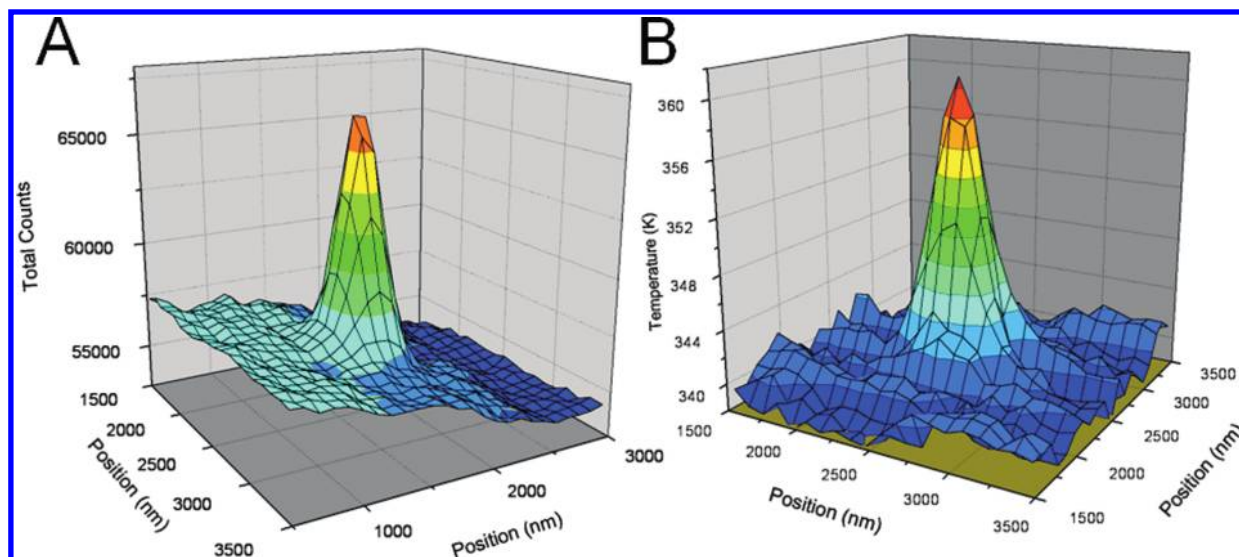
**Figure 2.** (A) Total photoluminescence of $Er^{3+}$ embedded in the film in the proximity of a 40 nm gold NP. (B) Temperature image of the NP shown in panel A created from the relative photoluminescence intensities.

imported into a software program (Image J) to determine the full width at half-maximum (fwhm) of the two-dimensional Gaussian laser profile. Equation 1 is used to determine the maximum laser intensity once the fwhm and laser power are known. Generally, the laser power is the integrated area under the two-dimensional Gaussian peak shape when the profile is plotted as a function of intensity and position. The laser intensity ($I_{laser}$) in eq 1 is chosen at the point where the Gaussian peak is a maximum

$$I_{laser} = \frac{P_{laser}(2.3546)^2}{2\pi(fwhm)^2} \qquad (1)$$

**Results.** Figure 1 is a diagram illustrating the properties of our thermal sensor. The laser excites a spot that depends upon the core size of the laser transmission fiber and numerical aperture of the microscope objective. Generally, we use a $50\times$ dark-field microscope objective with a numerical aperture of 0.80 that gives a two-dimensional Gaussian with a fwhm of ~800 nm. Excitation of a gold nanostructure with 532 nm light produces a hot spot whose temperature falls off as one over the distance. The photoluminescence spectrum from $Er^{3+}$ embedded in the thin film changes with temperature. Erbium emission from the hotter part of the hot spot has a spectrum where the photoluminescence intensity from the high energy peak ($^2H_{11/2} \rightarrow {}^4I_{15/2}$) is larger than the photoluminescence intensity from the low energy peak ($^4S_{3/2} \rightarrow {}^4I_{15/2}$). A colder relative temperature reverses this trend and the photoluminescence intensity from the low energy peak is larger than the photoluminescence intensity from the high energy peak (see Figure S1, Supporting Information). The collected photoluminescence is a weighted average of the photoluminescence collected over the entire sampled volume and the temperature extracted from the relative intensities represents a weighted average temperature from the sampled volume.

Figure 2A is the total photoluminescence from $Er^{3+}$ in the vicinity of a single 40 nm gold NP excited with a laser intensity of $1.73 \times 10^9$ W/m$^2$. The total photoluminescence is the sum of all the peak areas from $Er^{3+}$ emission and the total photoluminescence is enhanced by the gold NP. The percent enhancement % enhancement = [(peak height − baseline)/baseline] × 100%

is ~18%. The enhancement is because the plasmons from the gold NP interact with the dipole of the $Er^{3+}$ atoms causing an increase in the total photoluminescence. The enhancement should be most acute in the vicinity of the gold NP and should fall off with distance away from the NP. The 18% enhancement from the NP shown in Figure 2A would be significantly larger if the spatial resolution of the microscope was better and a smaller region around the NP sampled.

Figure 2B is the temperature image obtained from the relative photoluminescence intensities for the same NP collected with a laser intensity of $3.5 \times 10^{10}$ W/m$^2$. The temperature of film away from the NP rises because the $Al_{0.94}Ga_{0.06}N$/Er film is not totally transparent at 532 nm. The background temperature rise is a function of laser intensity. The difference is temperature between the background and peak maximum is easily obtained in the temperature image while the absolute temperature is more difficult to extract because the absolute temperature is dependent upon a parameter in our Boltzmann calibration ($y$-intercept). The intercept is chosen so that the temperature in the limit of no laser intensity is the ambient temperature of the film.

Figure 3A shows the temperature difference between the peak maximum and the background for the 40 nm gold NP as the laser intensity is changed (red data). The temperature difference is negative at low laser intensity and eventually becomes positive at elevated laser intensity. We believe that the negative temperature difference is not real but an artifact created because of the photoluminescence enhancement caused by the presence of the gold NP. The $Er^{3+}$ transition closest in energy to the gold NP plasmon ($^2H_{11/2} \rightarrow {}^4I_{15/2}$) is enhanced to a greater degree than the transition further away from the gold NP plasmon ($^4S_{3/2} \rightarrow {}^4I_{15/2}$). This nonuniform enhancement causes a depression in the "apparent" temperature that is corrected by moving the temperature difference until there is no temperature change at zero laser intensity. Interestingly, we find that temperature difference plots are usually linear with laser intensity. Figure 3B shows the absolute temperature plot for the data in Figure 3A. The background temperature shown in red is taken at a position far away from the NP. The intercept is adjusted to ensure that the background temperature limit at no laser intensity conformed to the ambient temperature.
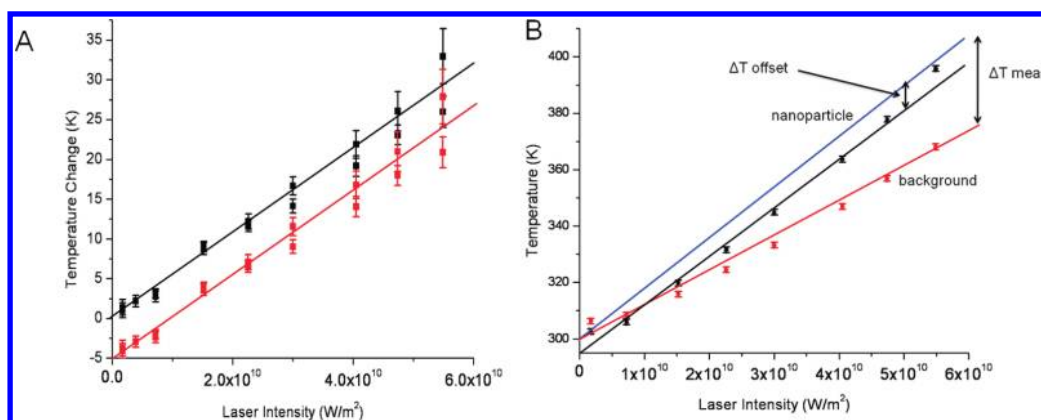
C

**Figure 3.** (A) Temperature change (shown as red data) from a 40 nm gold NP as a function of laser intensity. Corrected temperature change (shown as black data) for the data shown in red. The raw temperature change is moved with a constant offset to give a trend where the temperature change at a limit of no laser intensity is zero. (B) Absolute temperature for the background (red) and NP (black) as a function of laser intensity. The temperature offset from Figure 3A is added to the NP temperature (shown as the blue line) to give the corrected temperature of the NP.
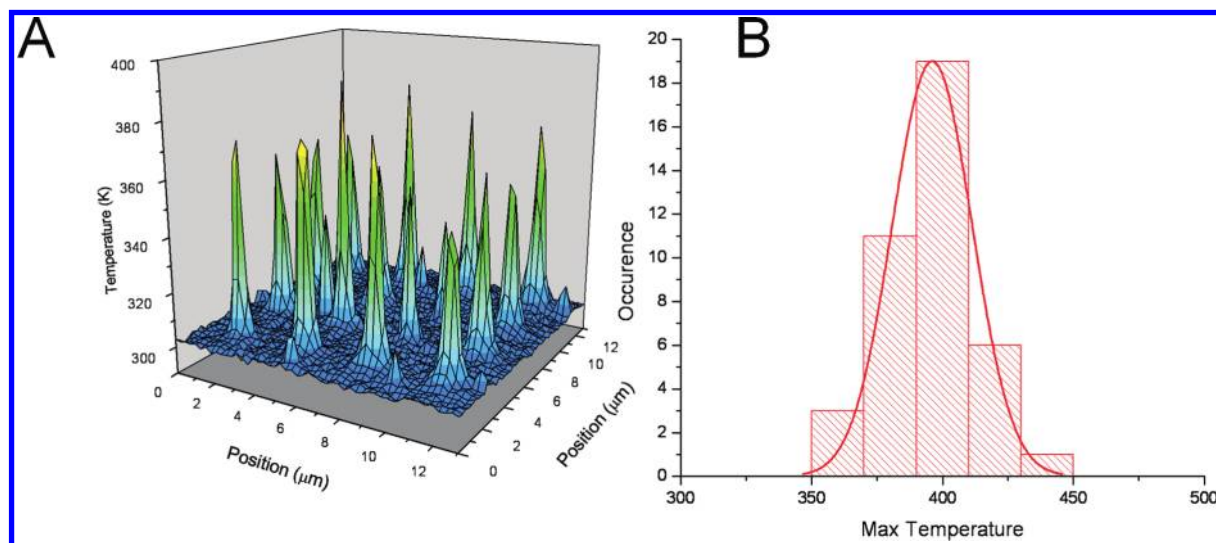


**Figure 4.** (A) Temperature image of $4 \times 4$ array of nanodots. The spacing between the nanodots is $3 \mu$m. The nanodots are excited with a laser intensity of $3.8 \times 10^{10}$ W/m$^2$. (B) Histogram of temperature for array of nanodots (subset of data shown in panel A). The distribution is fitted with a Gaussian profile with an average temperature of 390 K. The data was collected with a 50 $\mu$m bore size collection fiber.

The peak maximum data (shown in black) is where the gold NP is located. The same intercept was chosen for the background and peak maximum data. The blue line shows the result for the peak maximum data after correction the temperature with the offset correction shown in Figure 3A. The temperature axis errors bars were estimated from a fit of the temperature difference to a Gaussian peak shape. We estimate that the uncertainty in the laser intensity is $\pm 5 \times 10^8$ W/m$^2$ where the majority of the laser intensity uncertainty comes from our laser excitation spot size determination. A histogram of the temperature difference for multiple single 40 nm NPs shows a log-normal distribution with an average temperature difference of ~15 K (see Supporting Information, Figure S6).

A temperature image of a $4 \times 4$ array of nanodots is shown in Figure 4A. The $4 \times 4$ array is a subset of a larger array (shown in Figures S7,S8, Supporting Information). The spacing between the nanodots is $3 \mu$m. The nanodots are excited with a laser intensity of $3.8 \times 10^{10}$ W/m$^2$ and the photoluminescence is collected with a 50 $\mu$m collection fiber. AFM images of the nanodot (see Figure S8, Supporting Information) revealed some height variations. The average height is 71 nm with a 95% confidence interval

of 3.5 nm. Figure 4B is a histogram of temperature for the nanodots of Figure 4A. The temperature distribution conforms to a Gaussian shape where the average temperature change is 90 K and the histogram has a fwhm of ~45 K. Generally, we find that histograms of temperature have fwhm values ~one-half of the peak maximum value.

**Discussion.** *Temperature Transfer Parameter (ttp) Relating the Diffraction-Limited Average Measured Temperature to the Local Nonresolution-Limited Temperature.* The measured maximum temperature difference of a 40 nm NP as a function of laser intensity is shown in Figure 3A. The three parameters needed to calculate the local maximum temperature difference is absorption cross section, thermal conductivity, and the effective dielectric constant of the surrounding matrix. The thermal conductivity of the amorphous Al$_{0.94}$Ga$_{0.06}$N film ($k_{AlGaN}$) was measured with time-domain thermoreflectance[22,23] and found to be 1.5 $\pm$ 0.08 W/m-K.[24] The effective thermal conductivity of our system is $k_{eff} = [(k_{AlGaN} + k_{air})/2] \approx k_{AlGaN}/2$ or 0.75 $\pm$ 0.04 W/m-K. The effective dielectric constant is obtained[25] using eq 2 where $\varepsilon_b$ is the dielectric constant of air ($\varepsilon_b$ is 1), $\varepsilon_s$ is the dielectric constant of the
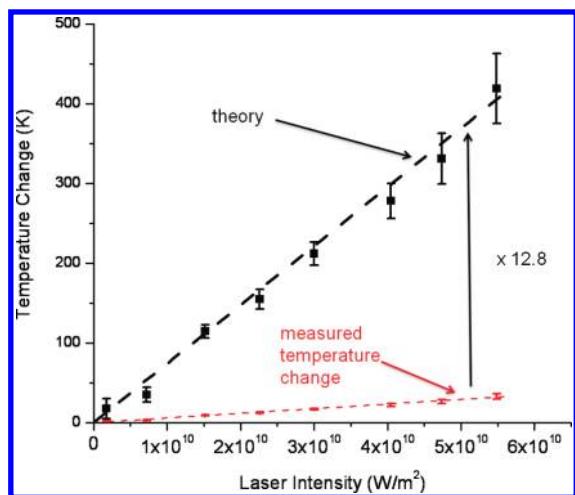
**Figure 5.** Temperature change of the 40 nm gold NP (shown in red) as a function of laser intensity. This data is reproduced from Figure 3A. This data is scaled by 12.8 to give the data (shown in black) that fits theory (shown as the black dash line) for the thermal behavior of a 40 nm gold NP.

substrate (Al$_{0.94}$Ga$_{0.06}$N film, $\varepsilon_s$ is 4), $\eta = [(\varepsilon_b - \varepsilon_s)/(\varepsilon_b + \varepsilon_s)] = -3/5$, $T_q^k = -0.25$ and $\gamma_q^k = 3$ for a spherical particle. This gives 1.12 as the effective dielectric constant for a spherical particle sitting on top of a substrate with dielectric constant 4 surrounded by air. This value for the effective dielectric constant is the same as the effective dielectric constant for a particle immersed in a homogeneous medium and is in reasonable agreement with scattering spectra collected from single gold NPs and nanodots (see Supporting Information, Figure S3).

$$\varepsilon_{eff} = \varepsilon_b \left( \frac{1 + \eta T_q^k/(1 + \gamma_q^k)}{1 + \eta T_q^k/(1 - \gamma_q^k)} \right) = 1.12 \qquad (2)$$

We use the absorption cross section ($C_{abs}$) of $1.4 \times 10^{-15}$ m$^2$ calculated using eq S1 (Supporting Information) for a single 40 nm gold NP immersed in an effective dielectric constant of 1.12.[48−50] The dielectric constant for bulk gold is used as the dielectric constant for the gold NP.[26] This value for the absorption cross section agrees with literature values for the absorption cross section calculated from Mie theory using our $\varepsilon_{eff}$.[11,27,28] Figure 5 shows the theoretical temperature change with laser intensity (using $C_{abs}$, $k_{eff}$, and $\varepsilon_{eff}$) compared to the measured temperature change. The slope of the plot for the theoretical temperature change with laser intensity ($\Delta T_{theory}/I_o$) is $7.4 \times 10^{-9} \pm 7.5 \times 10^{-10}$ m$^2$-K/W (see eq S9, Supporting Information).[51,52] The slope of the measured temperature change with laser intensity is $5.8 \times 10^{-10}$ m$^2$-K/W. The local absolute temperature of the 40 nm particle is obtained using $T_{local} = ttp\Delta T_{meas} + 300 + \Delta T_{back}$ where ttp is the temperature transfer parameter, $\Delta T_{meas} = (5.8 \times 10^{-10} \pm 2.7 \times 10^{-11})I_o$, and $\Delta T_{back} = (1.19 \times 10^{-9} \pm 1 \times 10^{-10})I_o$. The local temperature change per unit laser intensity ($\Delta T_{local}/I_o$) is found by subtracting the background and room temperature from the local temperature. The slope from the local and theoretical temperature change can be brought into alignment using a ttp of 12.8 with an uncertainty of ±0.6.

The ttp results because the true image size of the temperature profile from the hot nanostructure is much smaller that the collection volume that is sampled in the photoluminescence measurement. Also, we are collecting the average Er$^{3+}$ emission within the collection volume and converting this average photoluminescence spectrum into a temperature. This procedure results in an average temperature from the collection volume. The parameter ttp relates the measured average temperature to the NP surface temperature. We find that decreasing the collection volume by a factor of 2 increases the measured average temperature by a factor of 1.7 (see Supporting Information, Figure S5). The measured average temperature would be equal to the true temperature at the NP surface if there were sufficient spatial resolution. Interestingly, ttp appears to be invariant with laser intensity; see Figures 3, 5, and Supporting Information, Figure S5 where linear plots of temperature versus laser intensity are obtained. This suggests that our procedure for determining the local temperature (multiplying the measured temperature by ttp) can be applied under different conditions where different nanostructures are excited with different laser intensities. Also, the lack of spatial resolution affects the measurement in the enhancement of the photoluminescence signal by the gold NP. Better spatial resolution will increase the measured enhancement factor.

*Heat Generation, Temperature Change, and Melting of a Single Nanodot.* The temperature change of a single nanodot with laser intensity is shown in Figure 6. The nanodot has a height of ~71 nm with a width of ~120 nm (see Supporting Information, Figure S7). The measured temperature difference where the particle melts is ~80 K (see Figure 6). The local temperature for the melting point of the nanodot is expected to be nearly the same as the melting point for bulk gold (1343 K) because the size of the nanodot is large compared to a nanostructure size where melting point deviations are observed.[29] The laser intensity that induces melting of the nanodot is ~1.2 × 10$^{10}$ W/m$^2$. Melting of the nanodot is indicated by a deviation of linearity in the plot of temperature and laser intensity. The melted nanodot was irreversibly changed with an increase in absorption cross section. The melting of the nanodots was confirmed with scanning electron microscopy (SEM) (shown in the right panel of Figure 6). The nanodots on the left side of the panel where not irradiated with a laser intensity that induced melting while the dots on the right side were irradiated with a laser intensity sufficient to induce melting. The background temperature of the thermal sensor film is given by the equation ($T_{back} = (1.19 \times 10^{-9} \pm 1 \times 10^{-10})I_o$ and at the laser intensity that induces melting the background temperature is 314.3 ± 0.3 K. Using our value of 12.8 for ttp, the local temperature change is ~1024 K and the absolute temperature of the NP is 1338.3 K (1024 K + 314.3 K) which is in good agreement with the expected melting point of the gold nanodot.

*Size Estimate and Absorption Cross Section of a Single Nanodot.* The temperature change with laser intensity of a single nanodot with different collection fibers is shown in Figure S5 (Supporting Information). The slope of the temperature change with laser intensity ($\Delta T_{max}/I_o$) for a 25 $\mu$m collection fiber is $5.46 \times 10^{-9}$ m$^2$-K/W. This temperature can be scaled with our ttp (12.8) to give a local temperature slope $[\Delta T_{max}(ttp)]/I_o$ of $6.99 \times 10^{-8}$ m$^2$-K/W. The relationship between temperature change, size, and absorption cross section is given by $\Delta T_{max} = (C_{abs}^{ND}I_o)/(4\pi k_m R_{ND})$ where $R_{ND}$ is the radius of the nanodot and $C_{abs}^{ND}$ is the absorption cross section of the nanodot. The measured nanodot effective radius is 57.6 nm modeling the nanodot shape as a cylinder. This gives $3.8 \times 10^{-14}$ m$^2$ for the absorption cross section of the nanodot. The absorption
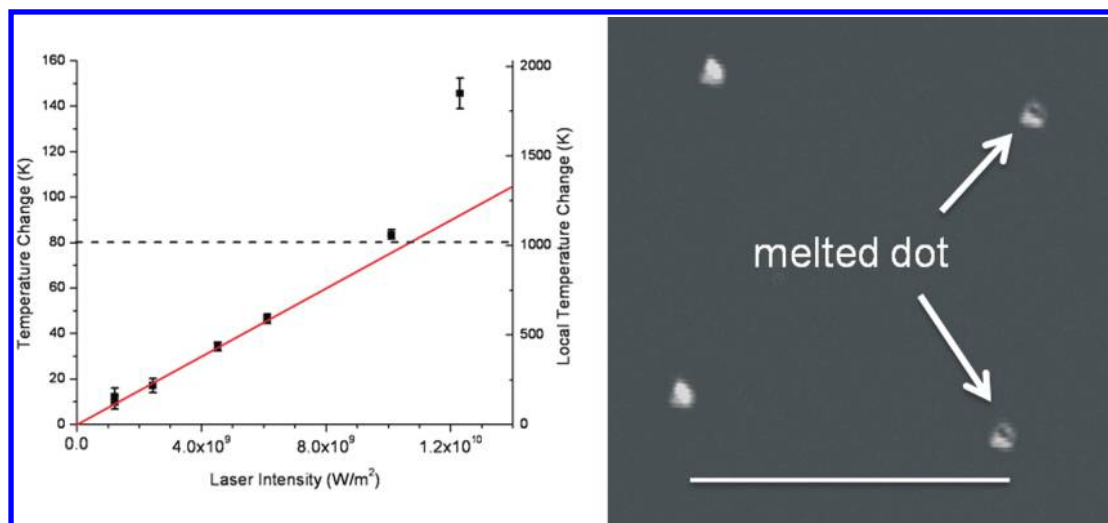
**Figure 6.** Temperature change of a nanodot as a function of laser intensity. The temperature axis on the left-hand side of the figure is the measured temperature change while the temperature axis on the right-hand side of the figure is the temperature deduced scaling between the diffraction limited temperature and the local nondiffraction limited temperature. The black dash line is the temperature change where bulk gold melts.

cross is expected to increases[27] as $R^3$ or $C_{abs}^{ND} = C_{abs}^{NP}(R_{ND}^3/R_{NP}^3)$ using the absorption cross section for the 40 nm NP as a reference. This gives an expected absorption cross section for the nanodot of $3.4 \times 10^{-14}$ m$^2$ in reasonable agreement with our result. It should be pointed out that this technique allows us to make a measurement of the absorption cross section of nanostructures with known size and shape. Measurements of single particle absorption cross sections also have been made by Vallee and Del Fatti.[8,30]

*Interface Conductance from a Single Optically Excited 40 nm NP.* The Fourier heat conduction theory works well when the heat carriers (electrons or phonons) excited by the heat-generating nanoparticle (nanoheater) can exchange energy efficiently with the surrounding medium. This happens when the phonon mean free path is shorter than the size of the nanoheater ensuring that there are enough scattering events to promote efficient energy exchange. If the phonon mean free path of the surrounding medium is larger than the nanoheater size then very few scattering events occur around the nanoheater and the heat transfer becomes ballistic.[1,3,31]

Interfacial properties can affect heat dissipation. Interfacial properties include both the effective dielectric constant and the interface conductance.[32−39] The effective dielectric constant is modulated by changes in the dielectric constant of interface materials. A small increase in the effective dielectric constant will increase the amount of heat generation because more light will be absorbed by the nanostructure. The thermal interface conductance changes the rate that heat is dissipated from a hot nanostructure to the surrounding matrix. The interfacial conductance has been relatively well characterized for colloidal nanostructures in aqueous and organic liquids.[40−42] An extension has been made to measure the interfacial conductance from water-covered hydrophobic and hydrophilic surfaces.[43] These results have been corroborated with theory where calculations of steady-state temperature profiles from small gold NPs (3 nm in diameter) in water and octane agree reasonably well with experiment.[44,45]

A critical interface conductance ($G_{critical}$) where the interface affects heat transport is given by eq 3.[41,45] In this equation, the thermal sensor matrix in air ($C_m$) and NP heat capacities ($C_{NP}$) are 1.20 and 2.49 J/K-cm$^3$ respectively; $k_m$ is the surrounding matrix thermal conductivity (0.75 W/m-K), and $G_{threshold}$ is ∼54

MW/m$^2$-K. Equation 3 provides an estimate where the temperature decay normally limited by heat diffusion into the surrounding matrix is limited by the thermal conductance through the interface. A temperature difference between the NP and sensor film ($\Delta T_{IC}$) will result if the interface conductance is less than or equal to 54 MW/m$^2$-K. If a discontinuous temperature results, then the interface conductance ($G$) can be calculated using eq 4 where $j_Q$ is the heat flux across the interface and $\Delta T_{IC}$ is the interfacial discontinuous temperature.

$$G_{critical} = \frac{3C_m k_m}{C_{NP} R_{NP}} \qquad (3)$$

$$j_Q = \frac{C_{abs} I_o}{4\pi R_{NP}^2} = G \Delta T_{IC} \qquad (4)$$

Figure 2A shows that a single 40 nm gold NP enhances the total Er$^{3+}$ photoluminescence. The percent enhancement with increasing laser intensity for a single 40 nm gold NP is shown in Figure 7. The percent enhancement decreases with laser intensity until it reaches a value around 14% where at a laser intensity of $3 \times 10^{10}$ W/m$^2$, the data shows a significant change in slope. We believe that this transition is due to the melting of the gold NP. The absorption cross section of melted NPs is different than solid NPs because of changes in effective dielectric constant.[46] The 40 nm NP melts at a temperature change of 1016 K.[29] The local temperature change of the surrounding film at a laser intensity of $3 \times 10^{10}$ W/m$^2$ is 210 K (see Figure 6). This gives a discontinuous temperature difference between the NP and the local film of 806 K. This temperature difference is designated as $\Delta T_{IC}$ where IC stands for interface conductance. We believe that the origin in the temperature difference comes from interfacial effects that limit heat transport to the sensor film. The heat flux is equal to the heat input ($C_{abs} I_o$) divided by the NP surface area $(4\pi R_{NP}^2)$. Using the absorption cross section of $1.4 \times 10^{-15}$ m$^2$ and intensity of $3 \times 10^{10}$ W/m$^2$, along with a discontinuous temperature of 806, gives an interface conductance of $10.4 \pm 0.4$ MW/m$^2$-K. The uncertainty in the interface conductance measurement assumes a 15% uncertainty in our local temperature
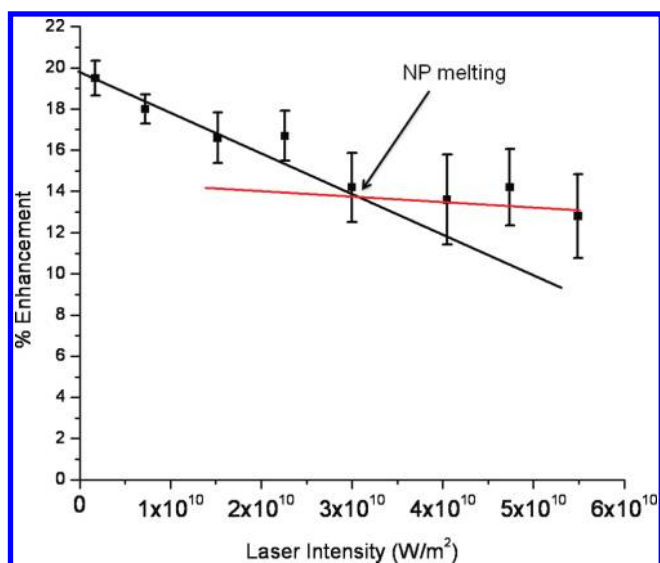
**Figure 7.** The percent enhancement in the $Er^{3+}$ photoluminescence from an interaction with a 40 nm gold NP as the laser intensity is changed. The percent enhancement decreases monotonically until a laser intensity $\sim 3 \times 10^{10}$ W/m$^2$ where a deviation is observed due to melting of the gold NP.



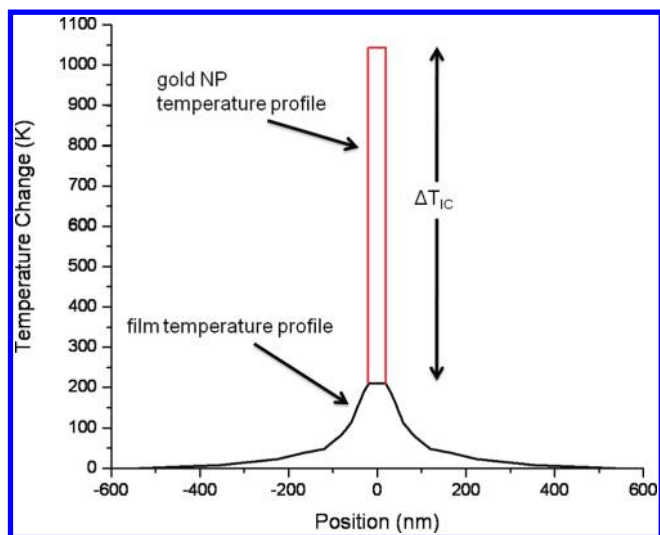**Figure 8.** Diagram showing the expected temperature profile around the 40 nm gold NP. A discontinuous temperature ($\Delta T_{IC}$) results with a temperature difference between the NP surface and sensor film. The sensor temperature falls off as one over distance away from the NP surface.

measurement. This leads to a local temperature change of $210 \pm 32$ K that gives a discontinuous temperature of $806 \pm 32$ K and ultimately an uncertainty of $\pm 0.4$ MW/m$^2$-K for the interface conductance.

Figure 8 presents a diagram for the local temperature profile of a 40 nm gold NP excited with a laser intensity of $3 \times 10^{10}$ W/m$^2$. The temperature profile is parallel to the thermal sensor surface ($x$ direction) while the same profile is expected in an orthogonal direction along the surface ($y$ direction) with a temperature drop having a $1/r$ dependence in the $z$ direction. The interfacial discontinuous temperature is labeled as $\Delta T_{IC}$ in the figure. There is a substantial discontinuity in temperature between the NP and the film in proximity to the NP.

Is an interface conductance of 10 MW/m$^2$-K for our system reasonable considering that the interface conductance of gold NPs in different solvents have already been measured?[41,47−52] Gold NPs in aqueous solutions have an interface conductance in the range of 100−130 MW/m$^2$-K whereas organic solvents such as toluene have a interface conductance an order of magnitude lower.[42] Also, heat dissipated from water-covered hydrophobic interfaces have a lower interface conductance ($G = 50$ MW/m$^2$-K) compared to water-covered hydrophilic interfaces ($G = 200$ MW/m$^2$-K).[43] Our surface ($Al_{0.94}Ga_{0.06}N$) is covered with air not water. Heat dissipation through air is expected to be minimal with the majority of the heat being dissipated through the surface. The initial surface is first covered with polylysine, making it hydrophilic, and then a layer of LC-sulfo-NHS-Biotin is added. Finally, 40 nm streptavidin covered Au NPs are attached to the surface. The NP now rests on a thermal insulating layer that semi-isolates the NP from the surface. An interface conductance around 10 MW/m$^2$-K is not unreasonable for a NP immobilized on a thermally insulating layer $\sim 5$ nm away from the surface.

If the heat dissipation is limited by interfacial effects for the 40 nm NP then does the interface limit heat transfer for the nano-dots as well. The critical interface conductance for the nanodot is 17 MW/m$^2$-K. The decrease in the critical interface conductance is because of the increase in size of the nanodot compared to the 40 nm NP. The nanodots are fabricated with e-beam lithography and sputtering resulting in a nanostructure that is intimately connected to the surface. The nanodots are strongly adhered to the surface because they survive the lift-off process. This strong surface adhesion increases, relative to the NP, the heat transfer to the surface. The increased interface conductance for the nanodot is believed to be above the critical interface conductance and a discontinuous temperature is not expected.

Finally, for processes where the surface temperature of the NP is important, (ligand attachment, photothermal therapy, or DNA melting, for example), and in regimes where interfacial effects control thermal transport, that is, the interface conductance is lower than the critical interface conductance, then the discontinuous temperature becomes an important parameter. In our measurement, we control the heat input and measure the temperature of the surrounding film. At steady-state, the heat input and dissipation to the surrounding must be equal. The nanodot was sufficiently large and intimately bonded to the surface that heat flow was not affected by the interface and the film temperature reasonably matched the NP temperature. In contrast, the interface conductance from the 40 nm NP is smaller than the critical interface conductance and a discontinuous temperature results. An analogy to this case is trying to fill a bucket with a hole in it. At steady-state, the rate that the bucket is filled must be equal to the rate that water is removed from the bucket. As the system approaches steady-state, the water level inside the bucket increases until the flow rate into and out of the bucket becomes equal. An independent measure of the NP temperature is needed to determine the discontinuous temperature. We use the melting temperature of the NP as the independent temperature measurement. We are able to determine the discontinuous temperature by measuring the film temperature at the laser intensity that causes melting. The interface conductance follows directly from the discontinuous temperature.

**Conclusions.** We have been able to show that a thin film of $Al_{0.94}Ga_{0.06}N$ embedded with $Er^{3+}$ ions can be used as an optical temperature sensor and that this thermal sensor can be used to image the temperature profile around optically excited gold

nanostructures. The sensor is calibrated to give the local temperature of a hot nanostructure by comparing the measured temperature change of a spherical 40 nm gold NP to the theoretical temperature change calculated from the absorption cross section. The calibration allows us to measure the temperature where a lithographically prepared gold nanodot melts, in agreement with the bulk melting point of gold, and the size of the nanodot, in agreement with SEM and AFM results. The 40 nm gold NPs cause an increase in the $Er^{3+}$ photoluminescence. The percent enhancement decreases linearly with laser power until it reaches a critical laser intensity where a transition is observed. We believe that the transition is caused by melting of the NP. This leads us to suspect that interfacial effects are affecting the heat dissipation of the hot NP. We determine an interface conductance of 10 MW/$m^2$-K by determining the discontinuous temperature using the melting point of a gold NP and measuring the film temperature where melting occurs.

## ■ ASSOCIATED CONTENT

**ⓢ Supporting Information.**　　This information includes $Er^{3+}$ photoluminescence spectra, AFM image of 40 nm gold NPs immobilized on the $Al_{0.94}Ga_{0.06}N$/Er thin film, calibration of the sensor with temperature, temperature difference of nanodots with different collection fibers, and characterization of nanodots with scattering spectra, SEM and AFM. This material is available free of charge via the Internet at http://pubs.acs.org.

## ■ AUTHOR INFORMATION

**Corresponding Author**
*E-mail: richards@helios.phy.ohiou.edu.

## ■ ACKNOWLEDGMENT

## ■ REFERENCES

(1) Chen, G. Ballistic-diffusive heat-conduction equations. *Phys. Rev. Lett.* **2001**, *86* (11), 2297–2300.

(2) Chen, G. Nonlocal and nonequilibrium heat conduction in the vicinity of nanoparticles. *J. Heat Transfer* **1996**, *118* (3), 539–545.

(3) Siemens, M. E.; Yang, R.; Nelson, K. A.; Anderson, E. H.; Murnane, M. M.; Kapteyn, H. C. Quasi-ballistic thermal transport from nanoscale interfaces observed using ultrafast coherent soft x-ray beams. *Nat. Mater.* **2010**, *9*, 26–30.

(4) Cahill, D. G.; Ford, W. K.; Goodson, K. E.; Mahan, G. D.; Majumdar, A.; Maris, H. J.; Merlin, R.; Phillpot, S. R. Nanoscale thermal transport. *J. Appl. Phys.* **2003**, *93* (2), 793–818.

(5) Carey, C. R.; Lebel, T.; Crisostomo, D.; Giblin, J.; Kuno, M.; Hartland, G. V. Imaging and Absolute Extinction Cross-Section Measurements of Nanorods and Nanowires through Polarization Modulation Microscopy. *J. Phys. Chem. C* **2010**, *114* (38), 16029–16036.

(6) Berciaud, S.; Cognet, L.; Blab, G. A.; Lounis, B. Photothermal heterodyne imaging of individual nonfluorescent nanoclusters and nanocrystals. *Phys. Rev. Lett.* **2004**, *93*, 25.

(7) Arbouet, A.; Christofilos, D.; Del Fatti, N.; Vallee, F.; Huntzinger, J. R.; Arnaud, L.; Billaud, P.; Broyer, M. Direct measurement of the single-metal-cluster optical absorption. *Phys. Rev. Lett.* **2004**, *93*, No. 127401.

(8) Muskens, O. L.; Bachelier, G.; Del Fatti, N.; Vallee, F.; Brioude, A.; Jiang, X. C.; Pileni, M. P. Quantitative Absorption Spectroscopy of a Single Gold Nanorod. *J. Phys. Chem. C* **2008**, *112* (24), 8917–8921.

(9) Berciaud, S.; Cognet, L.; Lounis, B. Luminescence decay and the absorption cross section of individual single-walled carbon nanotubes. *Phys. Rev. Lett.* **2008**, *101*, No. 077402.

(10) van Dijk, M. A.; Tchebotareva, A. L.; Orrit, M.; Lippitz, M.; Berciaud, S.; Lasne, D.; Cognet, L.; Lounis, B. Absorption and scattering microscopy of single metal nanoparticles. *Phys. Chem. Chem. Phys.* **2006**, *8* (30), 3486–3495.

(11) Giblin, J.; Syed, M.; Banning, M. T.; Kuno, M.; Hartland, G. Experimental Determination of Single CdSe Nanowire Absorption Cross Sections through Photothermal Imaging. *ACS Nano* **2010**, *4* (1), 358–364.

(12) Octeau, V.; Cognet, L.; Duchesne, L.; Lasne, D.; Schaeffer, N.; Fernig, D. G.; Lounis, B. Photothermal Absorption Correlation Spectroscopy. *ACS Nano* **2009**, *3* (2), 345–350.

(13) Lukianova-Hleb, E. Y.; Santiago, C.; Wagner, D. S.; Hafner, J. H.; Lapotko, D. O. Generation and detection of plasmonic nanobubbles in zebrafish. *Nanotechnology* **2010**, *21*, 22.

(14) Lukianova-Hleb, E.; Hu, Y.; Latterini, L.; Tarpani, L.; Lee, S.; Drezek, R. A.; Hafner, J. H.; Lapotko, D. O. Plasmonic Nanobubbles as Transient Vapor Nanobubbles Generated around Plasmonic Nanoparticles. *ACS Nano* **2010**, *4* (4), 2109–2123.

(15) Lapotko, D. Optical excitation and detection of vapor bubbles around plasmonic nanoparticles. *Opt. Express* **2009**, *17* (4), 2538–2556.

(16) Richardson, H. H.; Carlson, M. T.; Tandler, P. J.; Hernandez, P.; Govorov, A. O. Experimental and Theoretical Studies of Light-to-Heat Conversion and Collective Heating Effects in Metal Nanoparticle Solutions. *Nano Lett.* **2009**, *9* (3), 1139–1146.

(17) Richardson, H. H.; Thomas, A. C.; Carlson, M. T.; Kordesch, M. E.; Govorov, A. O. Thermo-optical responses of nanoparticles: Melting of ice and nanocalorimetry approach. *J. Electron. Mater.* **2007**, *36* (12), 1587–1593.

(18) Richardson, H. H.; Hickman, Z. N.; Govorov, A. O.; Thomas, A. C.; Zhang, W.; Kordesch, M. E. Thermooptical Properties of Gold Nanoparticles Embedded in Ice: Characterization of Heat Generation and Melting. *Nano Lett.* **2006**, *6* (4), 783–788.

(19) Gurumurugan, K.; Chen, H.; Harp, G. R.; Jadwisienczak, W. M.; Lozykowski, H. J. Visible cathodoluminescence of Er-doped amorphous AlN thin films. *Appl. Phys. Lett.* **1999**, *74* (20), 3008–3010.

(20) Dimitrova, V. I.; Van Patten, P. G.; Richardson, H.; Kordesch, M. E. Photo-, cathodo-, and electroluminescence studies of sputter deposited AlN: Er thin films. *Appl. Surf. Sci.* **2001**, *175*, 480–483.

(21) Garter, M. J.; Steckl, A. J. Temperature behavior of visible and infrared electroluminescent devices fabricated on erbium-doped GaN. *IEEE Trans. Electron Devices* **2002**, *49* (1), 48–54.

(22) Kang, K.; Koh, Y. K.; Chiritescu, C.; Zheng, X.; Cahill, D. G. Two-tint pump-probe measurements using a femtosecond laser oscillator and sharp-edged optical filters. *Rev. Sci. Instrum.* **2008**, *79*, 11.

(23) Cahill, D. G. Analysis of heat flow in layered structures for time-domain thermoreflectance. *Rev. Sci. Instrum.* **2004**, *75* (12), 5119–5122.

(24) Note: measured by Trong Tong and David Cahill, Materials Science and Engineering Department, University of Illinois at Urbana Champaign.

(25) Vernon, K. C.; Funston, A. M.; Novo, C.; Gomez, D. E.; Mulvaney, P.; Davis, T. J. Influence of Particle-Substrate Interaction on Localized Plasmon Resonances. *Nano Lett.* **2010**, *10* (6), 2080–2086.

(26) Johnson, P. B.; Christy, R. W. Optical-Constants Of Noble-Metals. *Phys. Rev. B* **1972**, *6* (12), 4370–4379.

(27) Jain, P. K.; Lee, K. S.; El-Sayed, I. H.; El-Sayed, M. A. Calculated Absorption and Scattering Properties of Gold Nanoparticles of Different Size, Shape, and Composition: Applications in Biological Imaging and Biomedicine. *J. Phys. Chem. B* **2006**, *110* (14), 7238–7248.

(28) Anderson, L. J. E.; Mayer, K. M.; Fraleigh, R. D.; Yang, Y.; Lee, S.; Hafner, J. H. Quantitative Measurements of Individual Gold Nanoparticle Scattering Cross Sections. *J. Phys. Chem. C* **2010**, *114* (25), 11127–11132.

(29) Buffat, P.; Borel, J. P. Size Effect On Melting Temperature Of Gold Particles. *Phys. Rev. A* **1976**, *13* (6), 2287–2298.

(30) Baida, H.; Billaud, P.; Marhaba, S.; Christofilos, D.; Cottancin, E.; Crut, A.; Lerme, J.; Maioli, P.; Pellarin, M.; Broyer, M.; Del Fatti, N.; Vallee, F. Quantitative Determination of the Size Dependence of Surface Plasmon Resonance Damping in Single Ag@SiO2 Nanoparticles. *Nano Lett.* **2009**, *9* (10), 3463–3469.

(31) Highland, M.; Gundrum, B. C.; Koh, Y. K.; Averback, R. S.; Cahill, D. G. Ballistic-phonon heat conduction at the nanoscale as revealed by time-resolved x-ray diffraction and time-domain thermoreflectance. *Phys. Rev. B* **2007**, *76*, 75337.

(32) Shenogina, N.; Godawat, R.; Keblinski, P.; Garde, S. How Wetting and Adhesion Affect Thermal Conductance of a Range of Hydrophobic to Hydrophilic Aqueous Interfaces. *Phys. Rev. Lett.* **2009**, *102*, No. 156101.

(33) Hu, M.; Keblinski, P.; Schelling, P. K. Kapitza conductance of silicon-amorphous polyethylene interfaces by molecular dynamics simulations. *Phys. Rev. B* **2009**, *79*, No. 104305.

(34) Watanabe, T.; Ni, B.; Phillpot, S. R.; Schelling, P. K.; Keblinski, P. Thermal conductance across grain boundaries in diamond from molecular dynamics simulation. *J. Appl. Phys.* **2007**, *102*, No. 063503.

(35) Angadi, M. A.; Watanabe, T.; Bodapati, A.; Xiao, X. C.; Auciello, O.; Carlisle, J. A.; Eastman, J. A.; Keblinski, P.; Schelling, P. K.; Phillpot, S. R. Thermal transport and grain boundary conductance in ultrananocrystalline diamond thin films. *J. Appl. Phys.* **2006**, *99*, No. 114301.

(36) Patel, H. A.; Garde, S.; Keblinski, P. Thermal Resistance of Nanoscopic Liquid-Liquid Interfaces: Dependence on Chemistry and Molecular Architecture. *Nano Lett.* **2005**, *5* (11), 2225–2231.

(37) Phillpot, S. R.; Schelling, P. K.; Keblinski, P. K. Interfacial thermal conductivity: Insights from atomic level simulation. *J. Mater. Sci.* **2005**, *40* (12), 3143–3148.

(38) Schelling, P. K.; Phillpot, S. R.; Keblinski, P. Kapitza conductance and phonon scattering at grain boundaries by simulation. *J. Appl. Phys.* **2004**, *95* (11), 6082–6091.

(39) Xue, L.; Keblinski, P.; Phillpot, S. R.; Choi, S. U. S.; Eastman, J. A. Two regimes of thermal resistance at a liquid-solid interface. *J. Chem. Phys.* **2003**, *118* (1), 337–339.

(40) Keblinski, P.; Prasher, R.; Eapen, J. Thermal conductance of nanofluids: is the controversy over?. *J. Nanopart. Res.* **2008**, *10* (7), 1089–1097.

(41) Ge, Z. B.; Cahill, D. G.; Braun, P. V. AuPd metal nanoparticles as probes of nanoscale thermal transport in aqueous solution. *J. Phys. Chem. B* **2004**, *108* (49), 18870–18875.

(42) Ge, Z. B. Nanoscale Thermal Transport at Solid-Liquid Interfaces. Ph.D. Thesis, University of Illinois at Urbana-Champaign, Urbana, 2006.

(43) Ge, Z. B.; Cahill, D. G.; Braun, P. V. Thermal conductance of hydrophilic and hydrophobic interfaces. *Phys. Rev. Lett.* **2006**, *96*, 18.

(44) Merabia, S.; Keblinski, P.; Joly, L.; Lewis, L. J.; Barrat, J. L. Critical heat flux around strongly heated nanoparticles. *Phys. Rev. E* **2009**, *79*, No. 021404.

(45) Merabia, S.; Shenogin, S.; Joly, L.; Keblinski, P.; Barrat, J. L. Heat transfer from nanoparticles: A corresponding state analysis. *Proc. Natl. Acad. Sci. U.S.A.* **2009**, *106* (36), 15113–15118.

(46) Lukianova-Hleb, E. Y.; Anderson, L. J. E.; Lee, S.; Hafner, J. H.; Lapotko, D. O. Hot plasmonic interactions: a new look at the photothermal efficacy of gold nanoparticles. *Phys. Chem. Chem. Phys.* **2010**, *12* (38), 12237–12244.

(47) Plech, A.; Kotaidis, V.; Gresillon, S.; Dahmen, C.; von Plessen, G. Laser-induced heating and melting of gold nanoparticles studied by time-resolved x-ray scattering. *Phys. Rev. B* **2004**, *70*, No. 195423.

(48) Link, S.; El-Sayed, M. A. Shape and size dependence of radiative, non-radiative and photothermal properties of gold nanocrystals. *Int. Rev. Phys. Chem.* **2000**, *19* (3), 409–453.

(49) Mulvaney, P. Surface Plasmon Spectroscopy of Nanosized Metal Particles. *Langmuir* **1996**, *12* (3), 788–800.

(50) Jain, P. K.; El-Sayed, I. H.; El-Sayed, M. A. Au nanoparticles target cancer. *Nano Today* **2007**, *2* (1), 18–29.

(51) Govorov, A. O.; Zhang, W.; Skeini, T.; Richardson, H.; Lee, J.; Kotov, N. A. Gold nanoparticle ensembles as heaters and actuators: melting and collective plasmon resonances. *Nanoscale Res. Lett.* **2006**, *1* (1), 84–90.

(52) Govorov, A. O.; Richardson, H. H. Generating heat with metal nanoparticles. *Nano Today* **2007**, *2* (1), 30–38.